

# Precise Anchoring of Fe Sites by Regulating Crystallinity of Novel Binuclear Ni-MOF for Revealing Mechanism of Electrocatalytic Oxygen Evolution

Xinqiang Liu, Shibiao Su, Haoran Yin, Shifan Zhang, Tayirjan Taylor Isimjan, Jin Huang,\*  
Xiulin Yang,\* and Dandan Cai\*

**Bimetallic metal-organic framework (BMOF) exhibits better electrocatalytic performance than mono-MOF, but deciphering the precise anchoring of foreign atoms and revealing the underlying mechanisms at the atomic level remains a major challenge. Herein, a novel binuclear NiFe-MOF with precise anchoring of Fe sites is synthesized. The low-crystallinity (LC)-NiFe<sub>0.33</sub>-MOF exhibited abundant unsaturated active sites and demonstrated excellent electrocatalytic oxygen evolution reaction (OER) performance. It achieved an ultralow overpotential of 230 mV at 10 mA cm<sup>-2</sup> and a Tafel slope of 41 mV dec<sup>-1</sup>. Using a combination of modulating crystallinity, X-ray absorption spectroscopy, and theoretical calculations, the accurate metal sequence of BMOF and the synergistic effect of the active sites are identified, revealing that the adjacent active site plays a significant role in regulating the catalytic performance of the endmost active site. The proposed model of BMOF electrocatalysts facilitates the investigation of efficient OER electrocatalysts and the related catalytic mechanisms.**

## 1. Introduction

In order to achieve the goal of “carbon peak” and “carbon neutralization”, the exploration of renewable and green energy has garnered significant attention. Hydrogen energy with zero-carbon emissions and high energy density is considered a potential energy carrier.<sup>[1]</sup> Electrocatalytic water splitting offers a promising strategy for producing high-purity hydrogen. However, its efficiency is severely limited by the sluggish kinetics of the anodic oxygen evolution reaction (OER).<sup>[2]</sup> Although IrO<sub>2</sub> and RuO<sub>2</sub> have been widely studied as commercial OER catalysts, their scarcity and high cost impede their industrial application.<sup>[3]</sup> Therefore, extensive efforts have been dedicated to developing low-cost and high performance alternatives to precious metal-based catalysts.

Metal-organic framework (MOF) is formed by coordination bonds between metal atom nodes and organic ligands with periodic structural units.<sup>[4]</sup> MOF have been widely applied in various fields including gas adsorption, separation, chemical sensors, drug delivery, and catalysis by their virtue of high porosity and multifunctionality.<sup>[5]</sup> Unfortunately, the electrocatalytic applications of MOF are hampered by poor electrical conductivity and blockage of active sites by organic ligands.<sup>[6]</sup> Various effective strategies such as metal doping,<sup>[7]</sup> morphological control,<sup>[8]</sup> facet engineering,<sup>[9]</sup> and lattice strain,<sup>[10]</sup> have been employed to improve electrocatalytic performance. For instance, Zhou et al.<sup>[7e]</sup> demonstrated that integrating hetero-metals into MOF for OER could enhance their electrocatalytic performance and provide insights into underlying mechanisms. Moreover, it is well-known that tri-metallic or dual-metallic MOF exhibit enhanced OER activities compared to single-metal MOF due to synergistic effects between hetero-metals, as supported by theoretical calculations and experimental observations.<sup>[11]</sup> However, the precise positions of foreign metals within MOF structure remain unclear, hindering the elucidation of underlying electrocatalytic mechanisms at the atomic level.

It is well-known that the reconstruction of MOF typically appears during OER.<sup>[12]</sup> The high-valence metal active sites are formed during self-reconstruction, which is conducive to improving catalytic activity.<sup>[13]</sup> Deliberately regulating the

X. Liu, S. Su, D. Cai  
School of Chemical Engineering and Technology  
Sun Yat-sen University  
Zhuhai 519082, P. R. China  
E-mail: caidd6@mail.sysu.edu.cn

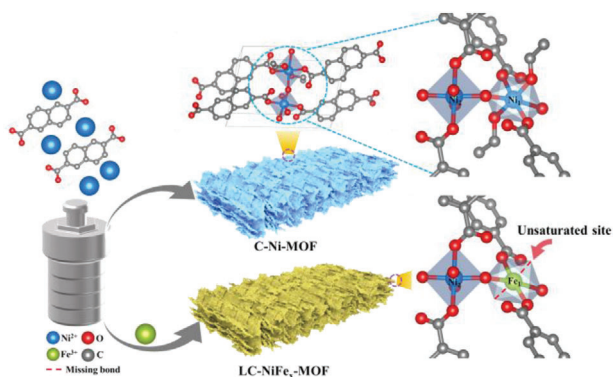
X. Liu, S. Su, H. Yin, S. Zhang, X. Yang, D. Cai  
Guangxi Key Laboratory of Low Carbon Energy Materials  
School of Chemistry and Pharmaceutical Sciences  
Guangxi Normal University  
Guilin 541004, P. R. China  
E-mail: xlyang@gxnu.edu.cn

T. T. Isimjan  
Saudi Arabia Basic Industries Corporation (SABIC)  
King Abdullah University of Science and Technology (KAUST)  
Thuwal 23955-6900, Saudi Arabia

J. Huang  
Pharmaceutical College  
Key Laboratory of Micro-Nanoscale Bioanalysis and Drug Screening of  
Guangxi Education Department  
Guangxi Medical University  
Nanning 530021, P. R. China  
E-mail: huangjin@mailbox.gxnu.edu.cn

The ORCID identification number(s) for the author(s) of this article can be found under <https://doi.org/10.1002/sml.202306085>

DOI: 10.1002/sml.202306085



**Scheme 1.** Synthesis scheme of LC–NiFe<sub>x</sub>–MOF ( $x = 0.25, 0.33, 0.50, 1.0$ ).

crystallinity of MOF is another crucial factor for improving OER electrocatalytic performance and understanding the corresponding mechanisms.<sup>[14]</sup> Specially, low-crystallinity or amorphous materials, which possess long-range disorder but short-range ordered structures, can accelerate the occurrence of the reconstruction.<sup>[15]</sup> Additionally, the structural flexibility of short-range ordered regions allows the materials to self-regulate and withstand structural disturbances during electrocatalysis, leading to obtain many unsaturated active sites.<sup>[16]</sup> Furthermore, coordinately unsaturated bonds with random orientation and aperiodic structures can facilitate electrocatalytic reactions by accelerating changes associated with intermediate bonding on the catalyst surface.<sup>[17]</sup> For example, Liu and co-workers reported low-crystallinity CoOOH nanosheet arrays (LC-CoOOH NAs/CFC) with short-range ordered grains obtained through an electrochemical strategy. LC-CoOOH NAs/CFC exhibited superior OER performance compared to high-crystallinity CoOOH NAs/CFC due to its abundant edge sites of CoOOH and oxygen vacancies.<sup>[18]</sup> Similarly, Huang's group achieved controllable amorphous engineering of bimetallic MOF, transitioning from crystalline to amorphous structures by adjusting the Co/Fe ratio. The resulting amorphous Co<sub>4</sub>Fe<sub>6</sub>-MOF demonstrated a low overpotential of 241 mV at 10 mA cm<sup>-2</sup> and a Tafel slope of 30.1 mV dec<sup>-1</sup>.<sup>[19]</sup> Unfortunately, MOF tend to adopt well-crystalline structures with infinite arrays and perfect symmetry due to the mutual matching of electron-withdrawing and electron-donating groups under fixed reaction conditions.<sup>[20]</sup> The active sites in well-crystalline MOF are confined within the framework, limiting the improvement of catalytic activities.<sup>[21]</sup> Therefore, developing effective strategies to regulate the crystallinity of bimetallic MOF to improve electrocatalytic performance and elucidate the OER electrocatalytic mechanism by precisely anchoring foreign atoms within the MOF structure is highly sought-after but challenging.

In this study, we achieved precise anchoring of Fe sites onto binuclear NiFe-MOF through structural evolution from well-crystallinity to low-crystallinity, induced by high-valence Fe ions. Thermal gravimetric analysis (TGA) and X-ray absorption spectroscopy (XAS) accurately confirmed that the Fe sites were located at the Ni<sub>1</sub> site of Ni-MOF. The introduction of high-valence Fe ions led to mismatched coordination between metal sites and ligands. This unique local architecture endowed the MOF with more available active sites and greatly improved charge trans-

fer. Density functional theory (DFT) calculations revealed that the atomically exposed Ni-Fe dual-metal sites actively participated in the OER process, optimizing the d-band center and binding strength of intermediates. Benefiting from the unique long-range disordered structure of low crystallinity, the optimized LC–NiFe<sub>0.33</sub>-MOF electrode exhibited superior OER performance with a low overpotential of 230 mV at a current density of 10 mA cm<sup>-2</sup> and a corresponding Tafel slope of 41 mV dec<sup>-1</sup>. This work not only provides a suitable approach to regulate the crystallinity of MOF but also offers a new strategy for precise anchoring of foreign atoms onto MOF and understanding the structure-activity relationship for electrocatalysis.

## 2. Results and Discussion

The synthetic procedure of C–Ni-MOF and LC–NiFe<sub>x</sub>-MOF is depicted in **Scheme 1**. Initially, metal ions (Ni<sup>2+</sup> and Fe<sup>3+</sup>) and 2,6-naphthalenedicarboxylic acid (NDA) organic ligands were mixed together in a solvent, resulting in a homogeneous solution.

It is important to note that the feeding ratio of Ni/Fe was maintained at 1:0.25, 1:0.33, 1:0.5, and 1:1. The LC–NiFe<sub>x</sub>-MOF ( $x = 0.25, 0.33, 0.5, 1.0$ ) was successfully synthesized through a one-step solvothermal process. The actual ratio of Ni and Fe in the LC–NiFe<sub>x</sub>-MOF samples was determined using inductively coupled plasma-mass spectroscopy (ICP-MS). The results indicated that the actual metal molar ratio in the products was consistent with the metal moles used in the synthesis (Table S1, Supporting Information). Crystalline single-metallic Ni-MOF (C–Ni-MOF) was also synthesized using a similar method to LC–NiFe<sub>x</sub>-MOF but without the addition of Fe ions.

Interestingly, the crystal structure of the as-synthesized C–Ni-MOF was simulated based on a known crystal structure of Co-MOF (CCDC no. 231755).<sup>[22]</sup> In the simulation, the metal centers Co and DMF ligands were substituted with Ni and ethanol, respectively. Furthermore, the structure information of C–Ni-MOF was obtained through Rietveld refinement of the corresponding powder X-ray diffractometry (PXRD) data. As shown in **Figure 1a**, the simulated structure of Ni-MOF exhibited a 3D structure. The Ni ions are coordinated by six O atoms in two different ways. The Ni<sub>1</sub><sup>2+</sup> ion was coordinated by six oxygen atoms, two from carboxylate ligands, two from H<sub>2</sub>O, and two from ethanol. The coordination environment of the Ni<sub>2</sub><sup>2+</sup> ion consisted of two oxygen atoms from carboxylate ligands and four O atoms from H<sub>2</sub>O molecules. The two Ni<sup>2+</sup> ions were bridged by a μ<sub>2</sub>-H<sub>2</sub>O molecule at the axis position. The refinement model was stable with low R-factors, as shown in **Figure 1b** and Table S2 (Supporting Information).

PXRD was conducted to analyze the phase transition and the degree of crystallinity evolution of the synthesized samples. **Figure 1b** provided further evidence that the structure of C–Ni-MOF, measured from the PXRD data, corresponded to our simulated Ni-MOF structure, indicating that the as-synthesized C–Ni-MOF possessed high crystallinity. In comparison, the main diffraction peaks of LC–NiFe<sub>x</sub>-MOF samples became weaker and exhibited a broad “hump” pattern, suggesting a decrease in crystallinity (**Figure 1c**). As the number of introduced Fe<sup>3+</sup> ions increased, the intensity of characteristic diffraction peaks showed a trend of weakening and then strengthening. When the molar ratio of Ni/Fe reached 1:0.33, the intensity of the diffraction

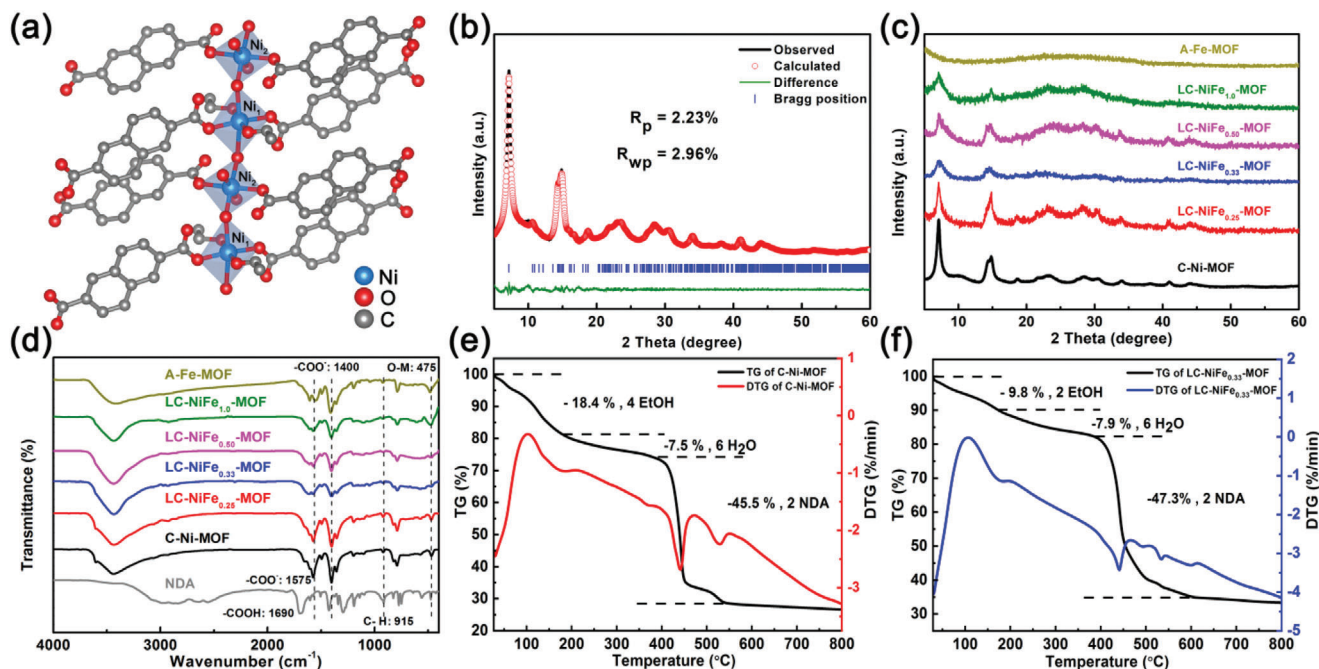


**Figure 1.** a) The coordination modes of the octahedral Ni atoms. b) Pawley refinement of PXR pattern of C–Ni–MOF. c) PXR patterns of C–Ni–MOF, A–Fe–MOF, and LC–NiFe<sub>x</sub>–MOF ( $x = 0.25, 0.33, 0.50,$  and  $1.0$ ). d) FT-IR spectra of NDA, C–Ni–MOF, A–Fe–MOF, and LC–NiFe<sub>x</sub>–MOF ( $x = 0.25, 0.33, 0.50$  and  $1.0$ ). TG and DTG curves of e) C–Ni–MOF and f) LC–NiFe<sub>0.33</sub>–MOF.

peaks was the lowest. In contrast, when Fe<sup>3+</sup> ions were solely coordinated with NDA ligands (forming A–Fe–MOF), the PXR patterns exhibited typical amorphous features. This phenomenon could be attributed to the disturbance of local electrons near the Ni<sup>2+</sup> center caused by the introduction of Fe<sup>3+</sup> ions.<sup>[20b]</sup> Therefore, the results confirmed that the precise anchoring of Fe sites onto the novel binuclear MOF was achieved through the introduction of high-valence Fe ions, leading to the formation of a low-crystallinity structure.

Fourier transform infrared (FT-IR) spectroscopy was conducted in the range of 4000–400 cm<sup>-1</sup> to detect the functional groups of C–Ni–MOF and LC–NiFe<sub>x</sub>–MOF. Figure 1d showed that the absorption peak at 1690 cm<sup>-1</sup> corresponded to the presence of protonated carboxyl groups (–COOH) in NDA.<sup>[23]</sup> Upon coordination, C–Ni–MOF and LC–NiFe<sub>x</sub>–MOF exhibited characteristic peaks at 1575 and 1400 cm<sup>-1</sup>, which were assigned to the asymmetric and symmetric stretching vibrations of coordinated carboxylate groups, respectively.<sup>[24]</sup> Additionally, the peak at 475 cm<sup>-1</sup> indicated the formation of M–O bonds between the carboxylic groups of NDA and Ni/Fe atoms.<sup>[25]</sup> These results confirmed the successful preparation of C–Ni–MOF and LC–NiFe<sub>x</sub>–MOF. Raman spectroscopy also provides similar results to FT-IR (Figure S1, Supporting Information).

To demonstrate the role of Fe<sup>3+</sup> in the low crystallization process, the metal source in the reaction was changed to Fe<sup>2+</sup> under the same Ni/Fe ratio, resulting in C–NiFe<sub>0.33</sub>–MOF. Figure S2a (Supporting Information) reveals that C–NiFe<sub>0.33</sub>–MOF shared a similar crystal phase with C–Ni–MOF, indicating that incorporating Fe<sup>2+</sup> into the framework did not alter its crystal structure. Raman spectra (Figure S2b, Supporting Information) confirms the coordination of the carboxylic group of NDA with Fe<sup>2+</sup> ions. This

experimental evidence highlighted the crucial role of anchoring Fe<sup>3+</sup> in the low crystallization process.

TGA was performed to examine the molecular structure and thermostability of C–Ni–MOF and LC–NiFe<sub>0.33</sub>–MOF. Figure 1e shows that C–Ni–MOF exhibited three weight losses at 18.4%, 7.5%, and 45.5% between 25 and 800 °C. Similarly, LC–NiFe<sub>0.33</sub>–MOF displayed three weight losses at 9.8%, 7.9%, and 47.3% (Figure 1f). The first weight loss (25–175 °C) corresponded to the removal of ethanol molecules. Interestingly, C–Ni–MOF lost four ethanol molecules, while LC–NiFe<sub>0.33</sub>–MOF lost only two. This suggested that the absence of coordinated ethanol ligands on the Ni<sub>1</sub> site in LC–NiFe<sub>0.33</sub>–MOF led to a local aperiodic arrangement of the framework.<sup>[20a]</sup> The second weight loss (175–388 °C) corresponded to the release of water molecules, and the third weight loss (388–550 °C) was attributed to the decomposition of NDA groups. And, the surface area of the samples, as determined by N<sub>2</sub> adsorption-desorption isotherms (Figure S3, Supporting Information), indicated an increase in surface area for LC–NiFe<sub>0.33</sub>–MOF. This suggested that the unsaturated material with a short-range ordered structure enhanced porosity, providing more accessible active sites and facilitating mass transfer during the electrocatalytic process.<sup>[26]</sup> This effect was further supported by electron paramagnetic resonance (EPR) analysis (Figure S4, Supporting Information), where LC–NiFe<sub>0.33</sub>–MOF exhibited a significant signal indicating the presence of unpaired electrons, while no detectable EPR signal was observed for C–Ni–MOF. Interestingly, the presence of unpaired electrons in MOF displayed the ability to increase the localization of metal 3d electrons near the Fermi level and generate unsaturated coordination active sites on the catalyst surface. These active sites played a crucial role in optimizing the adsorption and dissociation energy of oxygen-containing

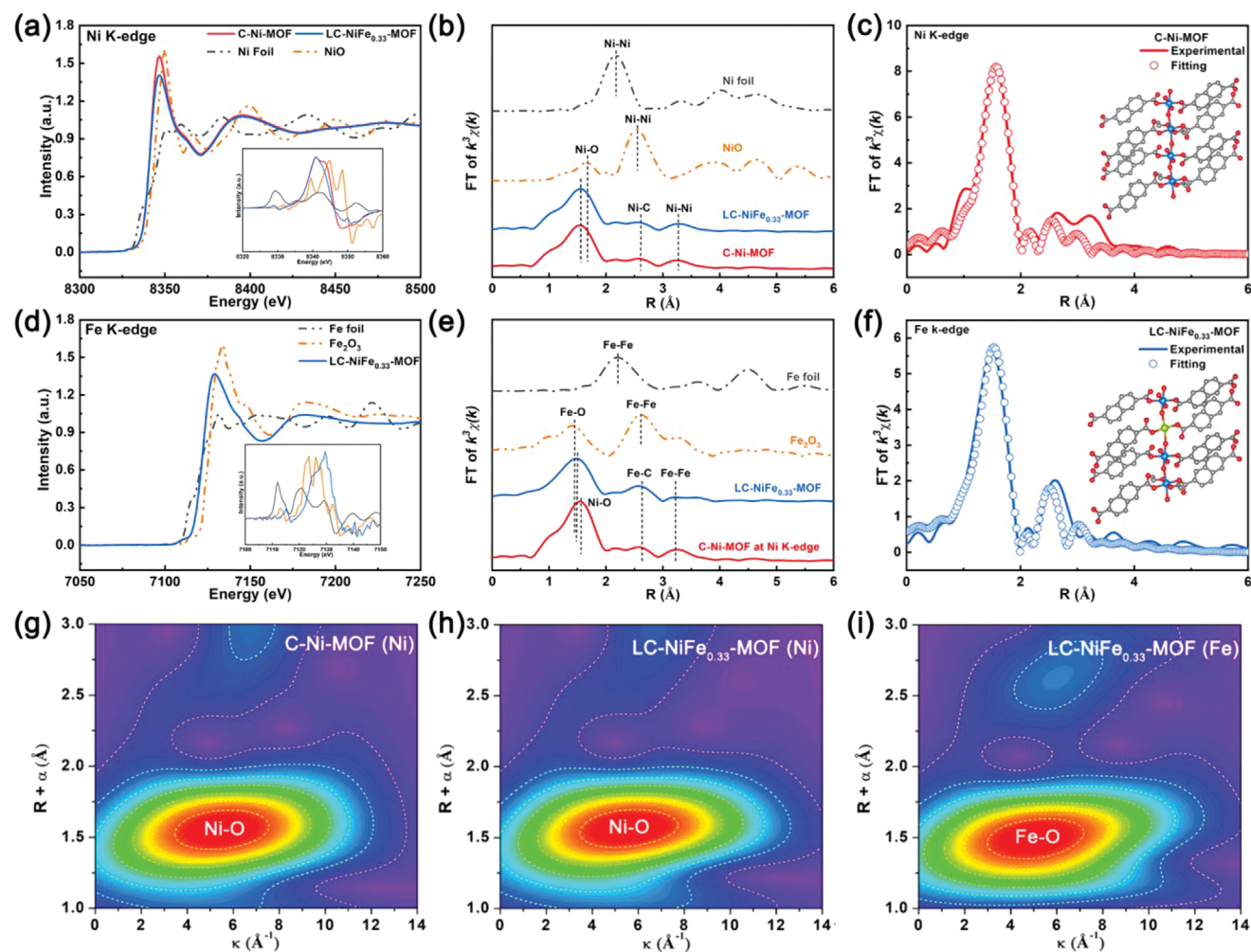


**Figure 2.** a) Ni K-edge XANES spectra, and b)  $k^3$ -weight EXAFS spectra Fourier-transformed EXAFS spectra of C-Ni-MOF, LC-NiFe<sub>0.33</sub>-MOF and their references. c) The magnitude fitting of Fourier transform R-space EXAFS (data-line and fit-circles) for C-Ni-MOF. d) Fe K-edge XANES spectra, and e)  $k^3$ -weight EXAFS spectra of LC-NiFe<sub>0.33</sub>-MOF and their references. f) The magnitude fitting of Fourier transform R-space EXAFS from various LC-NiFe<sub>0.33</sub>-MOF at Fe K-edge. g-i) WT-EXAFS of C-Ni-MOF and LC-NiFe<sub>0.33</sub>-MOF for Ni K-edge and Fe K-edge, respectively.

reactants, thereby significantly enhancing the catalytic activity of the material.<sup>[19]</sup>

X-ray photoelectron spectroscopy (XPS) was performed to investigate the surface chemical states and composition of the synthesized samples. The full XPS spectrum is presented in Figure S5 (Supporting Information). The high-resolution Ni 2p spectrum (Figure S6c, Supporting Information) indicated the presence of Ni<sup>2+</sup> oxidation state.<sup>[8b]</sup> The Ni 2p peaks of LC-NiFe<sub>0.33</sub>-MOF exhibited a low shift compared to C-Ni-MOF, suggesting a modification in the local electronic environment of Ni.<sup>[7e]</sup> In Figure S6d (Supporting Information), the characteristic peaks of LC-NiFe<sub>0.33</sub>-MOF at 711.6 eV (Fe 2p<sub>3/2</sub>) and 724.8 eV (Fe 2p<sub>1/2</sub>) corresponded to the Fe<sup>3+</sup> oxidation state.<sup>[27]</sup> These Fe peaks were shifted to higher binding energy compared to A-Fe-MOF. These XPS results showed the presence of a bimetallic synergistic effect in LC-NiFe<sub>0.33</sub>-MOF, which could influence the OER catalytic performance.<sup>[8d]</sup>

To further investigate the precise anchoring of Fe sites, synchrotron radiation XAS measurements were conducted.<sup>[28]</sup> The

Ni K-edge X-ray absorption near-edge structure (XANES) spectra of C-Ni-MOF and LC-NiFe<sub>0.33</sub>-MOF exhibited similar response signals, indicating identical chemical structures of Ni (Figure 2a). Notably, the white line intensity of LC-NiFe<sub>0.33</sub>-MOF was lower than that of C-Ni-MOF, indicating its lower crystallinity.<sup>[18]</sup> The first derivative XANES data (inset of Figure 2a) revealed that the  $E_0$  values (the first highest inflection point on the absorption edge) at the Ni K-edge of C-Ni-MOF and LC-NiFe<sub>0.33</sub>-MOF were both at 8341 eV, which was similar to NiO and significantly higher than Ni foil. This confirmed the valence state of Ni<sup>2+</sup>.<sup>[29]</sup> Additionally, the  $E_0$  value at the Fe K-edge of LC-NiFe<sub>0.33</sub>-MOF was close to Fe<sub>2</sub>O<sub>3</sub> (inset of Figure 2d) based on the first derivative XANES data, indicating that Fe in the sample had a similar valence state to Fe<sup>3+</sup> in Fe<sub>2</sub>O<sub>3</sub> and slightly higher than Fe<sub>2</sub>O<sub>3</sub>.<sup>[30]</sup> These XANES observations were consistent with the results obtained from the XPS analysis.

Fourier-transformed extended X-ray absorption fine structure (FT-EXAFS) spectroscopy in the R space was utilized without phase correction to analyze the samples. The obtained FT-EXAFS

spectra are presented in Figure 2b. The prominent peaks of both C–Ni–MOF and LC–NiFe<sub>0.33</sub>–MOF were observed at 1.56 Å, which was very close to the peak of NiO (1.65 Å) that had a [NiO<sub>6</sub>] octahedral building block. This suggested that the Ni atoms in C–Ni–MOF and LC–NiFe<sub>0.33</sub>–MOF possessed an octahedral coordination configuration.<sup>[31]</sup> Furthermore, the fitted EXAFS results of the R-space spectrum for C–Ni–MOF revealed that Ni atom was coordinated with six O atoms (Figure 2c; Figure S7 and Table S3, Supporting Information), consistent with the Rietveld refinement of PXRD data. The atomic arrangement of C–Ni–MOF is shown in Figure S9a (Supporting Information). Interestingly, the coordination number of LC–NiFe<sub>0.33</sub>–MOF was slightly reduced compared to C–Ni–MOF, and there was a slight shrinkage in the bond distance of the Ni–O bond itself after the introduction of Fe<sup>3+</sup> ions into the framework. This could be attributed to the smaller radius of Fe<sup>3+</sup> ions compared to Ni<sup>2+</sup> ions.<sup>[32]</sup> Additionally, the contracted Ni–O bond might also be influenced by the coordination between Fe<sup>3+</sup> ions and NDA ligands, potentially leading to long-range disorder. The M–M (M=Ni and Fe) peaks in both Ni and Fe K-edge EXAFS spectra of C–Ni–MOF and LC–NiFe<sub>0.33</sub>–MOF appeared longer compared to their respective reference materials due to the large size of NDA ligand, which affected the long distance between metal atoms and weakened the effective scattered signal between metals.<sup>[33]</sup> Moreover, the intensity of the Fe–O and Fe–Fe peaks was much lower than that of the Ni–O and Ni–Ni peaks (Figure 2e), indicating an increased degree of disorder upon the introduction of Fe<sup>3+</sup>.<sup>[20a]</sup> The first shell-fitted EXAFS results for LC–NiFe<sub>0.33</sub>–MOF revealed that Fe<sup>3+</sup> was coordinated with four oxygen atoms, suggesting a unique local environment for Fe<sup>3+</sup> (Figure 2f; Figure S8 and Table S4, Supporting Information).<sup>[11b]</sup> Combined with TGA data, it was confirmed that the chemical formula of LC–NiFe<sub>0.33</sub>–MOF contained two fewer ethanol molecules compared to C–Ni–MOF. This implied that the two ethanol molecules in LC–NiFe<sub>0.33</sub>–MOF originated from solvent guest molecules rather than coordinated ethanol. Therefore, the Fe<sup>3+</sup> ion was anchored at the sites of Ni<sub>i</sub> in the original framework and was only coordinated to two O atoms provided by NDA ligands and two additional O atoms from H<sub>2</sub>O, forming a coordinatively unsaturated site. The atomic structure arrangement of LC–NiFe<sub>0.33</sub>–MOF is revealed in Figure S9b (Supporting Information).

To gain more detailed insights into the local electronic structure, a wavelet transform (WT-EXAFS) was applied to the EXAFS results of Ni and Fe, allowing for simultaneous information analysis in both K space and R space. The WT contour plots revealed that LC–NiFe<sub>0.33</sub>–MOF exhibited a distinct intensity maximum compared to C–Ni–MOF, indicating a change in the coordination environment due to the presence of shortened Ni–O and Fe–O bonds (Figure 2g–i). The WT contour plot for Ni K-edge EXAFS of LC–NiFe<sub>0.33</sub>–MOF showed a strong maximum at ≈1.56 Å, while the Fe–O plot exhibited a slight downshift to ≈1.50 Å. These observations confirmed that the metal ions had successfully coordinated with the NDA ligands, and the introduction of Fe<sup>3+</sup> ions had the potential to influence the original structure of C–Ni–MOF, potentially leading to the formation of long-range disorder. Importantly, the altered coordination environment could impact the charge redistribution within the MOF, which played a crucial role in the catalytic activity of the OER process.<sup>[34]</sup>

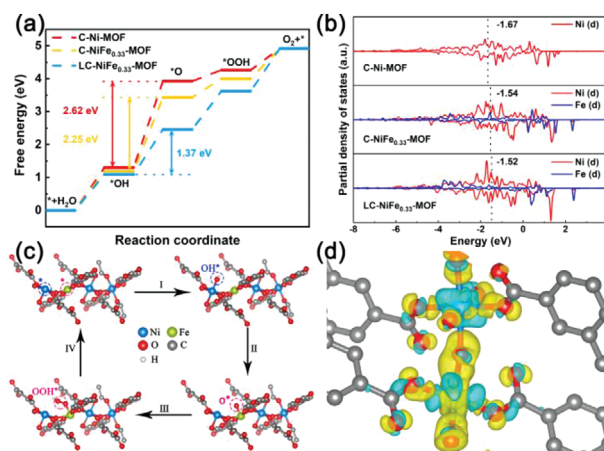


**Figure 3.** a) Gibbs free energy diagrams for OER progress on C–Ni–MOF, C–NiFe<sub>0.33</sub>–MOF and LC–NiFe<sub>0.33</sub>–MOF. b) PDOS of Ni and Fe active sites over the C–Ni–MOF, C–NiFe<sub>0.33</sub>–MOF, and LC–NiFe<sub>0.33</sub>–MOF. c) Elementary reaction steps of the OER process with the intermediates (OH\*, O\*, and OOH\*) on LC–NiFe<sub>0.33</sub>–MOF. d) Differential charge density diagram of LC–NiFe<sub>0.33</sub>–MOF (the cyan and yellow regions represent the depletion and accumulation of electrons, respectively).

The electron structure is an important factor in determining the performance of materials in electrocatalysis. Accurate and detailed research on the electronic structure and descriptors are of great significance for a deep understanding of the structure-activity relationship of materials.<sup>[32]</sup> To elucidate how the incorporation of unsaturated Fe<sup>3+</sup> sites and the synergistic effect between Ni modify the OER performance, systematic DFT calculations of pre-OER metal sites were performed for C–Ni–MOF, C–NiFe<sub>0.33</sub>–MOF, and LC–NiFe<sub>0.33</sub>–MOF.<sup>[35]</sup> The OER process typically involves four elementary steps: adsorption (steps I and III), dissociation (step II), and desorption (step IV) (Figure S10, Supporting Information). The formation of O\* was considered as the rate-determining step for the OER process in all samples. From Figure 3a, it could be observed that C–Ni–MOF exhibited a high  $\Delta G_2$  value of 2.62 eV. In contrast, C–NiFe<sub>0.33</sub>–MOF showed a decreased  $\Delta G_2$  of 2.25 eV, indicating that the presence of saturated Fe atoms could optimize electron transport and lower the reaction energy barrier. Importantly, LC–NiFe<sub>0.33</sub>–MOF displayed a further reduced  $\Delta G_2$  of 1.37 eV compared to C–Ni–MOF and C–NiFe<sub>0.33</sub>–MOF, suggesting that the synergy between dual-metallic sites enhances the OER activity. The adsorption capacity of OER intermediates was enhanced by promoting the central energy level of the *d*-band, which optimized the OER performance. This was further supported by the partial density of states (PDOS) analysis, which revealed changes in the electronic structure of Ni and Fe sites (Figure 3b). The *d*-band center of LC–NiFe<sub>0.33</sub>–MOF (–1.52 eV) was closer to the Fermi level than that of C–NiFe<sub>0.33</sub>–MOF (–1.54 eV) and C–Ni–MOF (–1.67 eV), indicating that LC–NiFe<sub>0.33</sub>–MOF possessed a stronger electron donation and acceptance capacity in the OER reaction.<sup>[36]</sup> As a result, LC–NiFe<sub>0.33</sub>–MOF exhibited a new electron state near the Fermi level.<sup>[7a]</sup> Furthermore, the Gibbs free energy ( $\Delta G$ ) was calculated for the OER intermediates (O\*, OH\*, and OOH\*) at two possible active sites (Ni and Fe sites) (Figure 3c). To explain the significantly reduced reaction energy barrier of

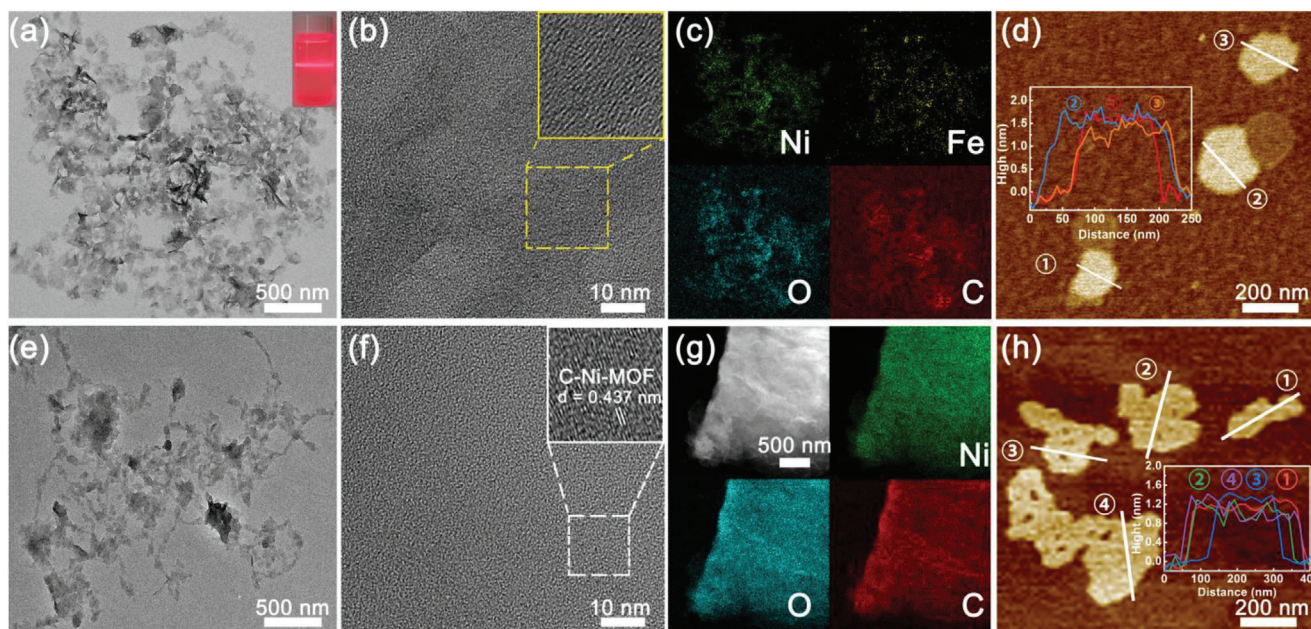


**Figure 4.** TEM images of a) LC-NiFe<sub>0.33</sub>-MOF and e) C-Ni-MOF, HR-TEM image of b) LC-NiFe<sub>0.33</sub>-MOF and f) C-Ni-MOF, the corresponding EDX elemental mapping images of c) LC-NiFe<sub>0.33</sub>-MOF and g) C-Ni-MOF, AFM images of d) LC-NiFe<sub>0.33</sub>-MOF and h) C-Ni-MOF.

LC-NiFe<sub>0.33</sub>-MOF, a detailed analysis of LC-NiFe<sub>0.33</sub>-MOF model was conducted. All possible adsorption sites for OH\*, O\*, and OOH\* were compared (Figure S11, Supporting Information). The rate-determining step was found to be the formation of O\* ( $\Delta G = 2.34$  eV) when Ni acted as the active site. The energy barriers for the OH\* and OOH\* steps were determined to be 1.09 and 0.59 eV, respectively. When Fe was simulated as the active site, the energy barriers for the formation of OH\* and OOH\* required of 0.62 and 1.17 eV, respectively. However, the free energy of O\* (1.83 eV) was found to be lower than that of the Ni site, indicating a lower rate-determining step in terms of theoretical overpotential. Therefore, for OH\*, the most stable adsorption site was identified as the Ni site. However, the high energy barrier hindered the formation of O\* on the Ni site, causing the O\* and OOH\* species to preferential transfer to adjacent Fe sites. This implied the presence of two types of active sites for activating intermediates in LC-NiFe<sub>0.33</sub>-MOF. Upon anchoring Fe<sup>3+</sup> sites to form a low-crystallinity material, abundant charge redistribution occurs in LC-NiFe<sub>0.33</sub>-MOF, with most of the charges clustering around the Fe<sup>3+</sup> sites. This facilitated subsequent electron transfer and absorption/desorption of intermediates (Figure 3d and Figure S12, Supporting Information).<sup>[37]</sup> This redistribution made the unsaturated Fe atoms in LC-NiFe<sub>0.33</sub>-MOF become active sites in addition to Ni atoms. In summary, the significant synergy between the two types of sites could be inferred from the DFT calculations in the LC-NiFe<sub>0.33</sub>-MOF catalyst, where Ni and Fe sites with different adsorption energies for intermediates participated in the OER process.

Transmission electron microscopy (TEM) was used to examine the morphology and structure of the synthesized products. Both LC-NiFe<sub>0.33</sub>-MOF and C-Ni-MOF exhibited cross-linked nanosheets morphology (Figure 4a,e), with LC-NiFe<sub>0.33</sub>-MOF showing a clear Tyndall effect under laser irradiation (in-

set of Figure 4a). Fourier transform filtering was applied to the high-resolution (HR)-TEM image. It revealed that no clear lattice fringes were observed in the HR-TEM image of LC-NiFe<sub>0.33</sub>-MOF, suggesting that it was composed of a group of short-range ordered grains with diverse orientations (Figure 4b), consistent with its low-crystallinity nature. In contrast, lattice fringe spacing was  $\approx 0.437$  nm for C-Ni-MOF, corresponding to the (102) lattice plane (Figure 4f). This indicated that C-Ni-MOF had a polycrystalline structure. TEM results further showed that C-NiFe<sub>0.33</sub>-MOF exhibited a long-range ordered polycrystalline structure (Figure S13, Supporting Information). Additionally, energy-dispersive X-ray (EDX) mapping confirmed the uniform distribution of elements in LC-NiFe<sub>0.33</sub>-MOF and C-Ni-MOF (Figure 4c and 4g). Atomic force microscopy (AFM) results (Figure 4d,h) showed that the average thickness of LC-NiFe<sub>0.33</sub>-MOF was 1–2 nm, confirming the ultrathin cross-linked nanosheets structure observed in scanning electron microscopy (SEM) images (Figure S14, Supporting Information). The crystal morphology was further analyzed using the Bravais-Friedel-Donnay-Harker (BFDH) method, which indicated that the 2D sheets morphology was in agreement with the experimental results (Figure S15, Supporting Information). The unique ultrathin multilayer configuration of the 2D nanomaterial facilitated abundant electronic channels for faster interfacial charge and mass transfer.<sup>[8b]</sup>

The electrocatalytic behavior of the synthesized samples for OER was evaluated using a typical three-electrode system in 1.0 M KOH electrolyte. Linear sweep voltammetry (LSV) measurements were performed at a scan rate of 5 mV s<sup>-1</sup>, and the data was corrected by 95% *i*R compensation to eliminate the influence of the ohmic potential drop. As shown in Figure 5a, the optimized LC-NiFe<sub>0.33</sub>-MOF electrode exhibited the lowest overpotential of 230 mV at a current density of 10 mA cm<sup>-2</sup>, compared to

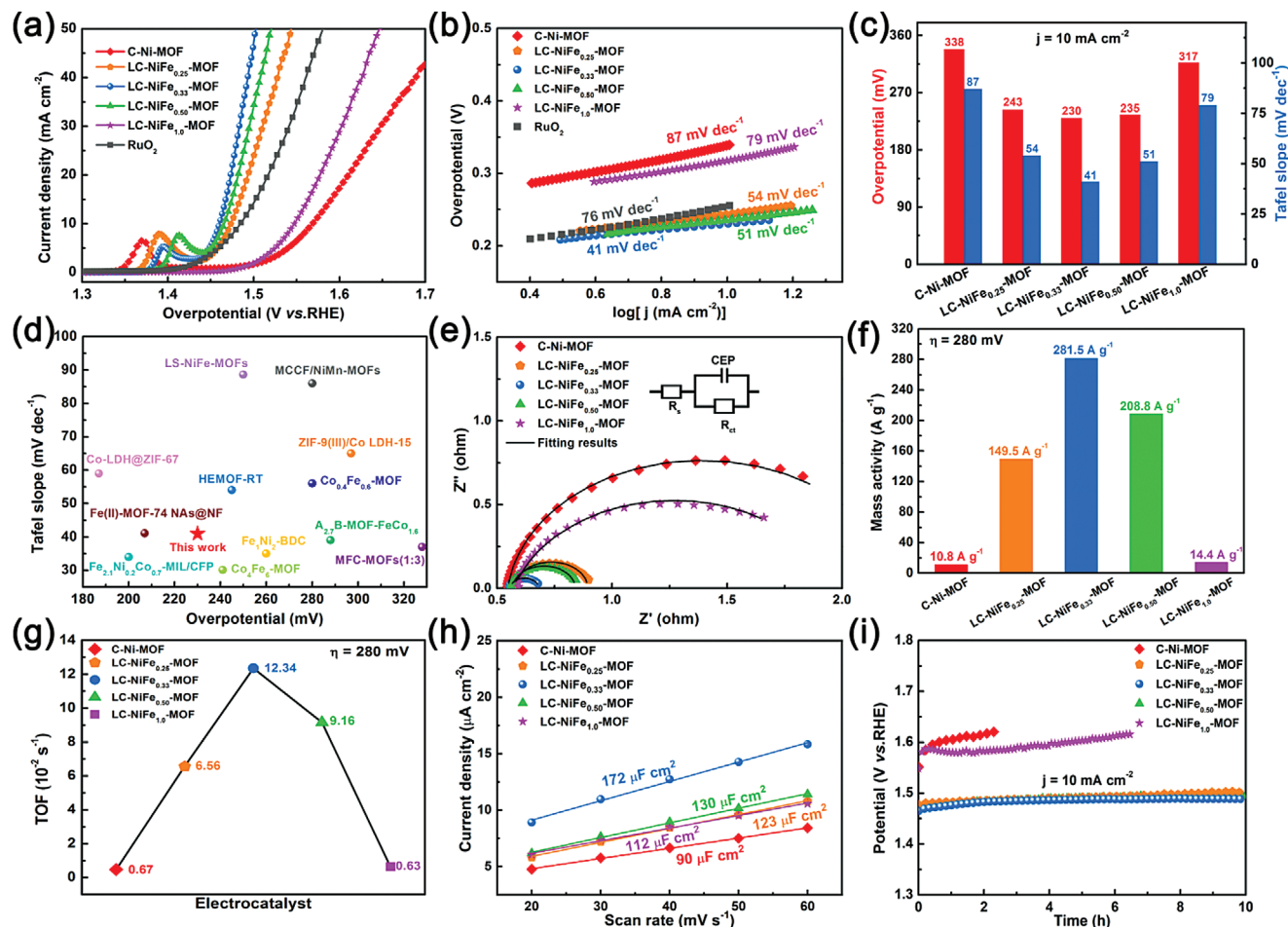


**Figure 5.** OER performance of the samples (C–Ni–MOF, LC–NiFe<sub>x</sub>–MOF  $x = 0.25, 0.33, 0.50,$  and  $1.0$ ) in  $1.0\text{ M KOH}$ . a) LSV curves with  $iR$ -compensated, b) the Tafel plots, c) comparison of the overpotentials at  $j = 10\text{ mA cm}^{-2}$  and the corresponding Tafel slopes, d) the overpotentials at  $10\text{ mA cm}^{-2}$  and their corresponding Tafel slopes of some previously reported catalysts, e) EIS curves at  $1.42\text{ V}$  versus RHE and fitting results for as-synthesized products, f) the mass activity values at overpotential of  $280\text{ mV}$ , g) the calculated TOF values at an overpotential of  $280\text{ mV}$ , h) the estimated  $C_{dl}$  values, and i) chronopotentiometric curves of long-term stability of electrodes in a constant current density of  $10\text{ mA cm}^{-2}$  without  $iR$  compensation.

C–Ni–MOF ( $338\text{ mV}$ ), LC–NiFe<sub>0.25</sub>–MOF ( $243\text{ mV}$ ), LC–NiFe<sub>0.50</sub>–MOF ( $235\text{ mV}$ ), LC–NiFe<sub>1.0</sub>–MOF ( $317\text{ mV}$ ), and C–NiFe<sub>0.33</sub>–MOF ( $280\text{ mV}$ , Figure S16, Supporting Information) and A–Fe–MOF (Figure S17, Supporting Information).

The Tafel slope as an indicator of the kinetics of the electrochemical OER process was also evaluated. Smaller Tafel slopes correspond to faster reaction rates. Figure 5b showed that LC–NiFe<sub>0.33</sub>–MOF exhibited the lowest Tafel slope value of  $41\text{ mV dec}^{-1}$ , compared to C–Ni–MOF ( $87\text{ mV dec}^{-1}$ ), LC–NiFe<sub>0.25</sub>–MOF ( $54\text{ mV dec}^{-1}$ ), LC–NiFe<sub>0.50</sub>–MOF ( $51\text{ mV dec}^{-1}$ ), and LC–NiFe<sub>1.0</sub>–MOF ( $79\text{ mV dec}^{-1}$ ), indicating favorable OER dynamics for the LC–NiFe<sub>0.33</sub>–MOF electrode. The overpotentials and Tafel slope for all samples are summarized in Figure 5c. Importantly, the LC–NiFe<sub>0.33</sub>–MOF catalyst outperformed many notable OER electrocatalysts in terms of overpotential and Tafel slope, as demonstrated in Figure 5d and Table S5 (Supporting Information).

The LC–NiFe<sub>0.33</sub>–MOF revealed the least semicircular diameter in comparison with other counterparts, disclosing the lowest charge transfer resistance and the best electron transport capa-

bility between electrode–electrolyte interfaces (Figure 5e). The reinforced reaction kinetics of LC–NiFe<sub>0.33</sub>–MOF was presumably related to the unique arrangement of atoms in the low-crystallinity structure and the synergistic effects between Ni<sup>2+</sup> and Fe<sup>3+</sup> ions. The electrode mass activity and turnover frequency (TOF) were applied to evaluate the quantitative parameters to assess the intrinsic activity of samples. The mass activity was calculated by the inverse proportion relation between current density and mass loading. The TOF values were based on the conception that all the metal centers of the catalyst would be considered active sites in the process of electrochemical.<sup>[38]</sup> The calculated data of as-synthesized materials exhibited volcanic characteristics in the following order LC–NiFe<sub>0.33</sub>–MOF > LC–NiFe<sub>0.50</sub>–MOF > LC–NiFe<sub>0.25</sub>–MOF > LC–NiFe<sub>1.0</sub>–MOF > C–Ni–MOF (Figure 5f,g).

The electrochemical active surface area (ECSA) of the samples was positively correlated with the double-layer capacitance ( $C_{dl}$ ) to further explain the intrinsic OER activity, and  $C_{dl}$  was evaluated based on cyclic voltammogram (CV) curves in a non-faradic region at gradual scan rate (Figure S18, Supporting Information). As seen from Figure 5h, the LC–NiFe<sub>0.33</sub>–MOF had

a higher  $C_{dl}$  ( $172 \mu\text{F cm}^{-2}$ ) than C–Ni–MOF ( $90 \mu\text{F cm}^{-2}$ ), LC–NiFe<sub>0.25</sub>–MOF ( $123 \mu\text{F cm}^{-2}$ ), LC–NiFe<sub>0.50</sub>–MOF ( $130 \mu\text{F cm}^{-2}$ ) and LC–NiFe<sub>1.0</sub>–MOF ( $112 \mu\text{F cm}^{-2}$ ), suggesting that LC–NiFe<sub>0.33</sub>–MOF possessed more accessible active sites. Furthermore, the prolonged stability was considered another crucial factor for pragmatic applications of electrocatalysts apart from the outstanding performance. Therefore, the chronopotentiometry (CP) curve was conducted to assess the durability of samples under the permanent current density of  $10 \text{ mA cm}^{-2}$ . The LC–NiFe<sub>0.33</sub>–MOF was well maintained after 10 h OER process at a constant current density of  $10 \text{ mA cm}^{-2}$ , demonstrating the high OER stability of LC–NiFe<sub>0.33</sub>–MOF in the catalytic process (Figure 5i).

The optimized LC–NiFe<sub>0.33</sub>–MOF owned favorable electrochemical activity, which could be attributed to the following reasons. After introducing Fe<sup>3+</sup> ions into the C–Ni–MOF, the LC–NiFe<sub>0.33</sub>–MOF could own multiple unsaturated sites and abundant charge transfer at an appropriate Ni/Fe ratio, therefore enhancing the OER performance of the above-mentioned catalysts. Meanwhile, the unique ultrathin cross-linked nanosheet structure of LC–NiFe<sub>0.33</sub>–MOF was advantageous to the spread of electrolytes and more rapid interfacial charge transfer. Besides, the synergistic reaction between Ni<sup>2+</sup> and Fe<sup>3+</sup> ions could accelerate the adsorption/desorption process of OER intermediates.

Considering the extraordinary OER activity of LC–NiFe<sub>0.33</sub>–MOF, the overall water splitting (OWS) system was assembled by LC–NiFe<sub>0.33</sub>–MOF as the anode and commercial Pt C<sup>−1</sup> as the cathode in 1.0 M KOH electrolyte (Figure S19a, Supporting Information). As shown in Figure S19b (Supporting Information), this device only needed a cell voltage of 1.54 V at  $10 \text{ mA cm}^{-2}$ . Simultaneously, this LC–NiFe<sub>0.33</sub>–MOF(+) || Pt/C(−) OWS system was compared to the newly reported cell voltage of the two-electrode devices at  $10 \text{ mA cm}^{-2}$ , suggesting that it outperforms most systems (Figure S19c and Table S6, Supporting Information). Moreover, this water electrolysis device could be stabilized for 120 h at  $100 \text{ mA cm}^{-2}$  with a voltage loss of 9.3%, revealing the outstanding stability of the LC–NiFe<sub>0.33</sub>–MOF catalyst (Figure S19d, Supporting Information). These results promised LC–NiFe<sub>0.33</sub>–MOF as a new type of electrocatalyst for practical OER in alkaline media.

To explore the microstructure transformation during the OER process, LC–NiFe<sub>0.33</sub>–MOF after OER test was probed by TEM, XRD, and XPS. Figure S20 (Supporting Information) depicts that the morphology of LC–NiFe<sub>0.33</sub>–MOF remained nanosheets after OER test. The corresponding EDX mapping revealed that Ni, Fe, O, and C elements were uniformly distributed after the OER test. There was variation in XRD patterns (Figure S21, Supporting Information), which contained the peaks of nickel hydroxide (JCPDS: 38–0715) and nickel oxide hydroxide (JCPDS: 06–0075), indicating the formation of (oxy)hydroxide under the OER operation.<sup>[39]</sup> The full XPS survey of LC–NiFe<sub>0.33</sub>–MOF exhibited the presence of C, O, F, S, Ni, and Fe elements after the OER test (Figure S22, Supporting Information). It was worth mentioning that the existence of S and F was derived from the addition of Nafion solution during the OER test. The spectrum of Ni 2p (Figure S23, Supporting Information) reflected that the peaks were shifted to higher binding energy (Ni 2p<sub>3/2</sub> at 857.2 eV) after the OER test compared to pristine MOF (Ni 2p<sub>3/2</sub> at 856.4 eV). More significantly, the new peaks could be derived from Ni<sup>3+</sup> with

binding energies of 859.3 and 879.0 eV, confirming the formation of NiOOH during the electrochemical process.<sup>[40]</sup>

To detect the evolution of MOF materials under the influence of electrolytes, the samples were immersed in electrolytes for 24 h. As shown in Figure S24 (Supporting Information), the diffraction peaks are present, indicating their high chemical stability. In addition, in-situ Raman was used to study the influence of external voltage and reconstruction mechanism of LC–NiFe<sub>0.33</sub>–MOF (Figure S25, Supporting Information). When the potential is 1.2 V versus RHE, the emerging peak near 427 and 663 cm<sup>−1</sup> was attributed to Fe–O vibration in FeOOH, and the rest of the two peaks at 479 and 525 cm<sup>−1</sup> were appointed to the E<sub>g</sub> bending vibration, and the A<sub>1g</sub> stretching vibration modes of Ni–O in Ni(OH)<sub>2</sub>. With increasing potential, the characteristic peaks of LC–NiFe<sub>0.33</sub>–MOF gradually disappeared and some new peaks belonging to metal hydroxides and oxyhydroxides were observed, suggesting a phase transition during the OER process.<sup>[41]</sup> Notably, the peak located at 525 cm<sup>−1</sup> blueshifted when the potential was applied to 1.4 V versus RHE. And, a peak at 552 cm<sup>−1</sup> could be assigned to NiOOH, revealing a partial transformation from hydroxide to oxyhydroxide, which coincided with the LSV data.<sup>[42]</sup> Those results suggested that LC–NiFe<sub>0.33</sub>–MOF suffered from surface reconstruction during the OER process and the in situ generated metal oxyhydroxides were the real active species for the electrocatalytic reaction.<sup>[34,39]</sup>

### 3. Conclusion

In this work, the precise anchoring of Fe sites was achieved by regulating the crystallinity of NiFe–MOF, and the intrinsic mechanism of transfer between Ni and Fe metal sites was investigated for OER. The experimental findings showed that the high-valence Fe ions were accurately anchored on the Ni<sub>1</sub> sites of the initial MOF, creating abundant unsaturated coordination sites. Additionally, a precise electronic model was constructed using DFT calculations to investigate the intrinsic mechanism of the synergistic interaction between Ni and Fe metal sites. The synergistic effect between the dual metal sites resulted in the effective tuning of the electronic structure. This tuning balanced the adsorption/desorption of intermediates and minimized the energy barrier for OER, thereby optimizing the intrinsic activity of the catalyst. The optimized LC–NiFe<sub>0.33</sub>–MOF exhibited a low overpotential of 230 mV at a current density of  $10 \text{ mA cm}^{-2}$  and a Tafel slope of 41 mV dec<sup>−1</sup>, surpassing the performance of RuO<sub>2</sub> and C–NiFe<sub>0.33</sub>–MOF. Overall, this work presented a new approach for tailoring the crystallinity of MOF and elucidated the electrocatalytic mechanism for OER. It provides valuable insights for the design and development of MOF-based electrocatalysts with enhanced performance in energy conversion and storage applications.

### Supporting Information

Supporting Information is available from the Wiley Online Library or from the author.

### Acknowledgements

X.L. and S.S. contributed equally to this work. This work was financially supported by the National Natural Science Foundation of China (No.

22068008, 21965005, 52363028), and Guangxi Province Natural Science Foundation (No. 2020GXNSFGA159104, 2019GXNSFGA245003)

## Conflict of Interest

The authors declare no conflict of interest.

## Data Availability Statement

Data sharing is not applicable to this article as no new data were created or analyzed in this study.

## Keywords

bimetallic metal-organic frameworks (BMOFs), crystallinity, electrocatalytic mechanism, oxygen evolution reaction, precise anchoring

Received: July 19, 2023  
Revised: September 25, 2023  
Published online:

- [1] H. Xie, Z. Zhao, T. Liu, Y. Wu, C. Lan, W. Jiang, L. Zhu, Y. Wang, D. Yang, Z. Shao, *Nature* **2022**, 612, 673.
- [2] a) F.-Y. Chen, Z.-Y. Wu, Z. Adler, H. Wang, *Joule* **2021**, 5, 1704; b) X. Wang, H. Zhong, S. Xi, W. S. V. Lee, J. Xue, *Adv. Mater.* **2022**, 34, 2107956; c) J. Zhou, Y. Dou, X.-Q. Wu, A. Zhou, L. Shu, J.-R. Li, *Small* **2020**, 16, 1906564.
- [3] a) K. Wang, X. Wang, Z. Li, B. Yang, M. Ling, X. Gao, J. Lu, Q. Shi, L. Lei, G. Wu, Y. Hou, *Nano Energy* **2020**, 77, 105162; b) K. Zhang, R. Zou, *Small* **2021**, 17, 2100129.
- [4] a) Q. Hou, Y. Wu, S. Zhou, Y. Wei, J. Caro, H. Wang, *Angew. Chem., Int. Ed.* **2019**, 58, 327; b) Q. Hou, S. Zhou, Y. Wei, J. Caro, H. Wang, *J. Am. Chem. Soc.* **2020**, 142, 9582.
- [5] a) G. Hai, H. Wang, *Coordin. Chem. Rev.* **2022**, 469, 214670; b) C.-P. Wang, Y.-X. Lin, L. Cui, J. Zhu, X.-H. Bu, *Small* **2023**, 19, 2207342.
- [6] a) S. Zhao, Y. Wang, J. Dong, C. T. He, H. Yin, P. An, K. Zhao, X. Zhang, C. Gao, L. Zhang, J. Lv, J. Wang, J. Zhang, A. M. Khattak, N. A. Khan, Z. Wei, J. Zhang, S. Liu, H. Zhao, Z. Tang, *Nat. Energy* **2016**, 118, 489; b) Z. Xue, K. Liu, Q. Liu, Y. Li, M. Li, C.-Y. Su, N. Ogiwara, H. Kobayashi, H. Kitagawa, M. Liu, G. Li, *Nat. Commun.* **2019**, 10, 5048.
- [7] a) Y.-T. Xu, Z.-M. Ye, J.-W. Ye, L.-M. Cao, R.-K. Huang, J.-X. Wu, D.-D. Zhou, X.-F. Zhang, C.-T. He, J.-P. Zhang, X.-M. Chen, *Angew. Chem., Int. Ed.* **2019**, 58, 139; b) Y. Sun, Z. Xue, Q. Liu, Y. Jia, Y. Li, K. Liu, Y. Lin, M. Liu, G. Li, C.-Y. Su, *Nat. Commun.* **2021**, 12, 1369; c) X.-L. Wang, L.-Z. Dong, M. Qiao, Y.-J. Tang, J. Liu, Y. Li, S.-L. Li, J.-X. Su, Y.-Q. Lan, *Angew. Chem., Int. Ed.* **2018**, 57, 9660; d) F.-L. Li, Q. Shao, X. Huang, J.-P. Lang, *Angew. Chem., Int. Ed.* **2018**, 57, 1888; e) W. Zhou, D.-D. Huang, Y.-P. Wu, J. Zhao, T. Wu, J. Zhang, D.-S. Li, C. Sun, P. Feng, X. Bu, *Angew. Chem., Int. Ed.* **2019**, 58, 4227.
- [8] a) K. Ge, S. Sun, Y. Zhao, K. Yang, S. Wang, Z. Zhang, J. Cao, Y. Yang, Y. Zhang, M. Pan, L. Zhu, *Angew. Chem., Int. Ed.* **2021**, 60, 12097; b) J. Huang, Y. Li, R.-K. Huang, C.-T. He, L. Gong, Q. Hu, L. Wang, Y.-T. Xu, X.-Y. Tian, S.-Y. Liu, Z.-M. Ye, F. Wang, D.-D. Zhou, W.-X. Zhang, J.-P. Zhang, *Angew. Chem., Int. Ed.* **2018**, 57, 4632; c) L. Zhuang, L. Ge, H. Liu, Z. Jiang, Y. Jia, Z. Li, D. Yang, R. K. Hocking, M. Li, L. Zhang, X. Wang, X. Yao, Z. Zhu, *Angew. Chem., Int. Ed.* **2019**, 58, 13565; d) F.-L. Li, P. Wang, X. Huang, D. J. Young, H.-F. Wang, P. Braunstein, J.-P. Lang, *Angew. Chem., Int. Ed.* **2019**, 58, 7051.
- [9] a) C. Wang, Q. Zhang, B. Yan, B. You, J. Zheng, L. Feng, C. Zhang, S. Jiang, W. Chen, S. He, *Nano-Micro Lett.* **2023**, 15, 52; b) J. Wan, D. Liu, H. Xiao, H. Rong, S. Guan, F. Xie, D. Wang, Y. Li, *Chem. Commun.* **2020**, 56, 4316; c) H. Zhao, L. Yu, L. Zhang, L. Dai, F. Yao, Y. Huang, J. Sun, J. Zhu, *ACS Sustainable Chem. Eng.* **2021**, 9, 10892.
- [10] a) W. Cheng, X. Zhao, H. Su, F. Tang, W. Che, H. Zhang, Q. Liu, *Nat. Energy* **2019**, 4, 115; b) Q. Ji, Y. Kong, C. Wang, H. Tan, H. Duan, W. Hu, G. Li, Y. Lu, N. Li, Y. Wang, J. Tian, Z. Qi, Z. Sun, F. Hu, W. Yan, *ACS Catal.* **2020**, 10, 5691.
- [11] a) C. Wu, X. Zhang, H. Li, Z. Xia, S. Yu, S. Wang, G. Sun, *Chinese J. Catal.* **2021**, 42, 637; b) X. Zhao, B. Pattengale, D. Fan, Z. Zou, Y. Zhao, J. Du, J. Huang, C. Xu, *ACS Energy Lett.* **2018**, 3, 2520; c) J. Yang, Y. Shen, Y. Sun, J. Xian, Y. Long, G. Li, *Angew. Chem., Int. Ed.* **2023**, 135, e202302220.
- [12] J. Ding, D. Guo, N. Wang, H.-F. Wang, X. Yang, K. Shen, L. Chen, Y. Li, *Angew. Chem., Int. Ed.* **2023**, 62, e202311909.
- [13] a) A. Grimaud, A. Demortière, M. Saubanière, W. Dachraoui, M. Duchamp, M.-L. Doublet, J.-M. Tarascon, *Nat. Energy* **2017**, 2, 17002; b) X. Liu, J. Meng, K. Ni, R. Guo, F. Xia, J. Xie, X. Li, B. Wen, P. Wu, M. Li, J. Wu, X. Wu, L. Mai, D. Zhao, *Cell Rep Phys Sci* **2020**, 1, 100241.
- [14] J. Ding, T. Fan, K. Shen, Y. Li, *Appl Catal B* **2021**, 292, 120174.
- [15] a) W. Cai, R. Chen, H. Yang, H. B. Tao, H.-Y. Wang, J. Gao, W. Liu, S. Liu, S.-F. Hung, B. Liu, *Nano Lett.* **2020**, 20, 4278; b) Q. Wu, M. S. Siddique, Y. Guo, M. Wu, Y. Yang, H. Yang, *Appl Catal B* **2021**, 286, 119950.
- [16] a) T. Guo, L. Li, Z. Wang, *Adv. Energy Mater.* **2022**, 12, 2200827; b) J. Liu, L. Guo, *Matter* **2021**, 4, 2850.
- [17] S. Shen, Z. Wang, Z. Lin, K. Song, Q. Zhang, F. Meng, L. Gu, W. Zhong, *Adv. Mater.* **2022**, 34, 2110631.
- [18] S. Ye, J. Wang, J. Hu, Z. Chen, L. Zheng, Y. Fu, Y. Lei, X. Ren, C. He, Q. Zhang, J. Liu, *ACS Catal.* **2021**, 11, 6104.
- [19] X. Hou, Z. Han, X. Xu, D. Sarker, J. Zhou, M. Wu, Z. Liu, M. Huang, H. Jiang, *Chem. Eng. J.* **2021**, 418, 129330.
- [20] a) J. Li, W. Huang, M. Wang, S. Xi, J. Meng, K. Zhao, J. Jin, W. Xu, Z. Wang, X. Liu, Q. Chen, L. Xu, X. Liao, Y. Jiang, K. A. Owusu, B. Jiang, C. Chen, D. Fan, L. Zhou, L. Mai, *ACS Energy Lett.* **2018**, 4, 285; b) T. D. Bennett, A. K. Cheetham, *Acc. Chem. Res.* **2014**, 47, 1555.
- [21] a) C. Liu, J. Wang, J. Wan, Y. Cheng, R. Huang, C. Zhang, W. Hu, G. Wei, C. Yu, *Angew. Chem., Int. Ed.* **2020**, 59, 3630; b) X. Zhang, G. Li, Y. Zhang, D. Luo, A. Yu, X. Wang, Z. Chen, *Nano Energy* **2021**, 86, 106094.
- [22] H. Xu, Z. Xu, *Micropor. Mesopor. Mat.* **2012**, 157, 33.
- [23] D. Senthil Raja, C.-L. Huang, Y.-A. Chen, Y. Choi, S.-Y. Lu, *Appl Catal B* **2020**, 279, 119375.
- [24] J. Duan, S. Chen, C. Zhao, *Nat. Commun.* **2017**, 8, 15341.
- [25] J. Jia, L. Wei, F. Li, C. Yu, K. Yang, T. Liang, *Inorg Chem* **2021**, 128, 108605.
- [26] Y. Dang, P. Han, Y. Li, Y. Zhang, Y. Zhou, *J. Mater. Sci.* **2020**, 55, 13951.
- [27] F. Li, Y. Tian, S. Su, C. Wang, D.-S. Li, D. Cai, S. Zhang, *Appl Catal B* **2021**, 299, 120665.
- [28] L.-M. Cao, J. Zhang, L.-W. Ding, Z.-Y. Du, C.-T. He, *J. Energy Chem* **2022**, 68, 494.
- [29] J.-R. Huang, X.-F. Qiu, Z.-H. Zhao, H.-L. Zhu, Y.-C. Liu, W. Shi, P.-Q. Liao, X.-M. Chen, *Angew. Chem., Int. Ed.* **2022**, 61, e202210985.
- [30] J. Han, X. Meng, L. Lu, J. Bian, Z. Li, C. Sun, *Adv. Funct. Mater.* **2019**, 29, 1808872.
- [31] W. Cheng, X. F. Lu, D. Luan, X. W. (D.) Lou, *Angew. Chem., Int. Ed.* **2020**, 59, 18234.
- [32] Y. Li, M. Yuan, H. Yang, K. Shi, Z. Sun, H. Li, C. Nan, G. Sun, *Appl Catal B* **2023**, 323, 122167.
- [33] D. Friebel, M. W. Louie, M. Bajdich, K. E. Sanwald, Y. Cai, A. M. Wise, M.-J. Cheng, D. Sokaras, T.-C. Weng, R. Alonso-Mori, R. C. Davis, J. R.

- Bargar, J. K. Nørskov, A. Nilsson, A. T. Bell, *J. Am. Chem. Soc.* **2015**, *137*, 1305.
- [34] S. Zhao, C. Tan, C.-T. He, P. An, F. Xie, S. Jiang, Y. Zhu, K.-H. Wu, B. Zhang, H. Li, J. Zhang, Y. Chen, S. Liu, J. Dong, Z. Tang, *Nat. Energy* **2020**, *5*, 881.
- [35] Y. Liu, X. Li, S. Zhang, Z. Wang, Q. Wang, Y. He, W.-H. Huang, Q. Sun, X. Zhong, J. Hu, X. Guo, Q. Lin, Z. Li, Y. Zhu, C.-C. Chueh, C.-L. Chen, Z. Xu, Z. Zhu, *Adv. Mater.* **2023**, *35*, 2300945.
- [36] Z. Zhang, X. Li, C. Zhong, N. Zhao, Y. Deng, X. Han, W. Hu, *Angew. Chem., Int. Ed.* **2020**, *59*, 7245.
- [37] Y. Niu, X. Teng, S. Gong, Z. Chen, *J. Mater. Chem. A* **2020**, *8*, 13725.
- [38] J. Tian, F. Jiang, D. Yuan, L. Zhang, Q. Chen, M. Hong, *Angew. Chem., Int. Ed.* **2020**, *59*, 13101.
- [39] L. Zhang, J. Wang, K. Jjiang, Z. Xiao, Y. Gao, S. Lin, B. Chen, *Angew. Chem., Int. Ed.* **2022**, *61*, e202214794.
- [40] Q. Qian, Y. Li, Y. Liu, L. Yu, G. Zhang, *Adv. Mater.* **2019**, *31*, 1901139.
- [41] Y.-J. Wu, J. Yang, T.-X. Tu, W.-Q. Li, P.-F. Zhang, Y. Zhou, J.-F. Li, J.-T. Li, S.-G. Sun, *Angew. Chem., Int. Ed.* **2021**, *60*, 26829.
- [42] W. Peng, A. Deshmukh, N. Chen, Z. Lv, S. Zhao, J. Li, B. Yan, X. Gao, L. Shang, Y. Gong, L. Wu, M. Chen, T. Zhang, H. Gou, *ACS Catal.* **2022**, *12*, 3743.